Particle Aggregation with Simultaneous Surface Growth

Pablo Mitchell* and Michael Frenklach†
Department of Mechanical Engineering, University of California at Berkeley, Berkeley, CA 94720-1740
(Dated: April 29, 2003)

Particle aggregation with simultaneous surface growth was modeled using a dynamic Monte Carlo method. The Monte Carlo algorithm begins in the particle inception zone and constructs aggregates via ensemble-averaged collisions between spheres and deposition of gaseous species on the sphere surfaces. Simulations were conducted using four scenarios. The first, referred to as scenario 0, is used as a benchmark and simulates aggregation in the absence of surface growth. Scenario 1 forces all balls to grow at a uniform rate while scenario 2 only permits them to grow once they have collided and stuck to each other. The last one is a test scenario constructed to confirm conclusions drawn from scenarios 0–2. The transition between the coalescent and the fully-developed fractal aggregation regimes is investigated using shape descriptors to quantify particle geometry. They are used to define the transition between the coalescent and fractal growth regimes. The simulations demonstrate that the morphology of aggregating particles is intimately related to both the surface deposition and particle nucleation rates.

PACS numbers: 61.43.Hv,83.10.Rs,83.10.Tv

I. INTRODUCTION

Transformation of gas into particulate matter is at the core of a variety of natural phenomena and industrial processes; examples may include formation of atmospheric fog [1, 2], combustion soot [3, 4], interstellar dust [5, 6], carbon black [7], and commodity ceramics like fumed silica and pigmentary titania [8]. Conventional description of the particulate inception begins with homogeneous nucleation of precursors in the gas phase, leading to the appearance of the first recognizable particles. These *primary* particles are assumed to be spherical and collisions among them coalescent, i.e., forming larger spherical particles. In the case of solid particulates, the collected samples often exhibit characteristics of fractal-like aggregates [9–12]. It is understood therefore that the initial period of coalescent growth must transition to particle aggregation [3]. Surface deposition also contributes to particle growth. Gas phase species attach themselves to the surface of the particles during both the coalescent and aggregation stages of formation. This adds a layer of mass on the particle surface. Surface growth encourages a rounder shape and counters the geometric randomness added by aggregation.

Among all the processes, coalescent coagulation is understood the most. Formulated by Smoluchowski [13], the underlying system of differential equations was largely solved by the mid-70s [1, 2, 14]. Those developments were largely focussed on liquid aerosols, motivated by the growing concerns of atmospheric pollution. The methodology was adopted to the description of solid particulates (e.g., [3, 8, 15]) addressing the emerging interest in material powder synthesis and the striker requirements for controlling particulate emission from combustion sources.

The new applications emphasized further what already was known from prior developments, namely, the importance of coupling between nucleation and coagulation dynamics. The new analysis and size-resolved numerical simulations revealed that the particle size distribution function (PSDF) is affected by the rate of nucleation [16–18]. For a strong nucleation source, PSDF is entirely dominated by the smallest particles.

Surface growth received less attention since it is usually argued that the formation of primary particles consumes all of the gaseous precursors leaving no gas-phase material for deposition onto the particle surface [8, 19]. In the case of soot formation, much of the solid-phase material (up to 80%) is generated via surface deposition [20]. The present understanding indicates that the chemical reactions controlling growth of gaseous precursors are analogous to reactions underlying surface growth [21].

While the formation of particle aggregates is well documented and their fractal-like appearance is well characterized (see, e.g., the references cited above), the transition between the formation of primary particles and chain-like aggregates is not well understood. One theory [22–28] postulates that particles are composed of viscous matter which coalesce completely at small sizes. As the particle size increases they do not have sufficient time to fuse. Often referred to as *sintering*, it is used in tandem with coagulation to model particle formation in the vapor phase. While sintering may be an appropriate model for formation of materials such as silicon [29, 30], it provides a less convincing argument when applied to materials such as carbonaceous soot. Indeed, carbon materials cannot melt, like silicon does. Soot particles formed during hydrocarbon combustion have a turbostratic structure [3]. While sintering of such particles could be envisioned as motion of turbostratic units, electron microscopy typically reveals multi-particle composi-

*pablo.mitchell@cal.Berkeley.EDU
†myf@ME.Berkeley.EDU

tion of primary particles [3, 32].

Another theory states that the nearly spherical shape of primary particles is the result of surface growth accompanied by aggregation [3, 31–33]. The transition is caused by the cessation of surface growth, when the smoothing effects of surface growth do not hide the characteristics of particles added by the aggregation process.

Irrespective of differences in views on how primary particles are formed, it has been generally presumed that particle aggregation is separated in time from nucleation and surface growth. An extensive theoretical analysis was carried out on the problem of aggregate formation from a presumed ensemble of primary particles [34–38]. It has been shown that aggregates begin to behave in a fractal-like manner when they are significantly larger than their constituent primary particles.

Meakin demonstrated fractal behavior by showing that the aggregate radius of gyration, R_g, scaled with its number of primary particles, n, through the power-law $R_\mathrm{g} \sim n^{1/D_\mathrm{f}}$, where D_f is the fractal dimension [39]. This relationship is often written in the form

$$n = k_\mathrm{f} \left(R_\mathrm{g}/R_\mathrm{p}\right)^{D_\mathrm{f}} \tag{1}$$

where k_f is a constant fractal prefactor [35]. This result has been useful in analysis of fractal characteristics of "mature" powder samples and their optical properties [9, 11, 12, 40, 41], but is insufficient to address the dynamics of transition from coalescent growth to aggregation in the presence of surface growth.

Our recent dynamic Monte Carlo simulations demonstrated that aggregation of spherical particles with simultaneous surface growth can lead to a spheroidal shape [42]. The simulations were performed for the conditions of a laminar premixed flame and follow the history of an individual particle, referred to as the *collector*. The analysis attributed the spheroidal shape of the growing aggregate to rapid surface growth and intense particle nucleation. For the particle geometry to become spheroidal, the surface growth determined by the gaseous flame environment must be capable of burying particles stuck to the collector surface. If they are too large, even the flame's maximum surface growth rate may not be sufficient to bury them quickly enough. Smaller particles, on the other hand, are more easily covered. This couples particle aggregation not only to surface growth but also to particle nucleation, since, as mentioned above, only in the presence of a strong nucleation source particle distribution is dominated by the smallest particles.

In the present study we examine the transition from particle coalescence to aggregation, identify factors controlling the phenomenon, and develop a method of predicting when this transition occurs. The assumed model includes surface growth but no sintering. The analysis is perform in very general terms, not limited to a particular system.

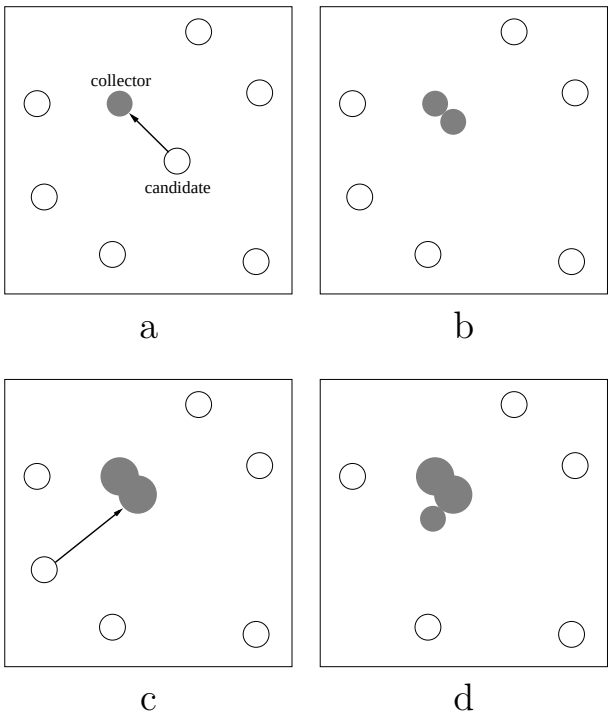

FIG. 1: Four step particle growth algorithm: (a) starts by immersing the collector in an ensemble of primary particles and surface growth species; (b) a candidate particle is chosen and translated along a random trajectory where it collides and sticks on impact; (c) the elapsed time of the collision is computed and the collector particle grows uniformly over that time interval; (d) the entire process, steps a–c, is repeated.

II. MODEL

Particle aggregation with simultaneous surface growth is modeled using a dynamic Monte Carlo method. A single solid particle, the *collector*, is immersed in the *Environment*, an inexhaustible ensemble of spherical primary particles and gaseous surface growth species (FIG. 1a). Mathematically, each primary particle is modeled with a ball in $\mathbb{R}^3$. The model begins in the particle inception zone where the collector is allowed to grow via ensemble-averaged collisions with primary particles and deposition of gaseous species on its surface. Then a primary particle, referred hereafter as the *candidate*, is chosen and translated along a randomly generated ballistic trajectory towards the collector. Candidate particles collide with the collector one at a time and stick on impact without rearrangement (FIG. 1b). Next, the elapsed time of each collision (Δt) is calculated [42, 43]. The collector surface grows uniformly via surface deposition during Δt (FIG. 1c). At this point the process repeats itself until the simulation terminates. Further details of this model are given in [42]; an in-depth description and numerical implementation can be found in [44].

III. SHAPE DESCRIPTORS

Any discussion of collector geometry must be accompanied by meaningful measures with which to make quantitative comparisons. To meet the objectives of the present study, such measures have to clearly characterize the particle roundness, commensurate with visual assessment from experimental observations. The same parameters should prove useful in predicting when and why the particle growth transitions from the coalescent regime to fully-developed fractal aggregation.

Recalling that aggregates are modeled with a union of balls, we require a descriptor to measure the amount of intersection between them. In effect, the descriptor must differentiate between chain-like and spheroidal aggregates.

A. Fractal dimension

Our first inclination might be to use the fractal dimension, D_f. However, inspection of the numerical results displayed in FIG. 2 suggests that D_f alone is not sufficient to quantify geometric differences between aggregates. D_f fails as a measure of roundness. Comparing FIG. 2a and FIG. 2b reveals two markedly different aggregates but with nearly identical fractal dimensions, $D_\mathrm{f} \approx 3$. This clearly demonstrates that D_f cannot differentiate between chain-like and spheroidal aggregates. In fact, a suitable shape descriptor should attribute closer values to the aggregates in FIG. 2b and 2c. Both of these particles exhibit granular behavior and no intersection. Yet, they do not share the same fractal behavior since the one in FIG. 2c has $D_\mathrm{f} = 1.03$. It is not essential that we differentiate between varying modes of fractal behavior. We only require a shape descriptor capable of distinguishing between the coalescent and fractal growth regimes.

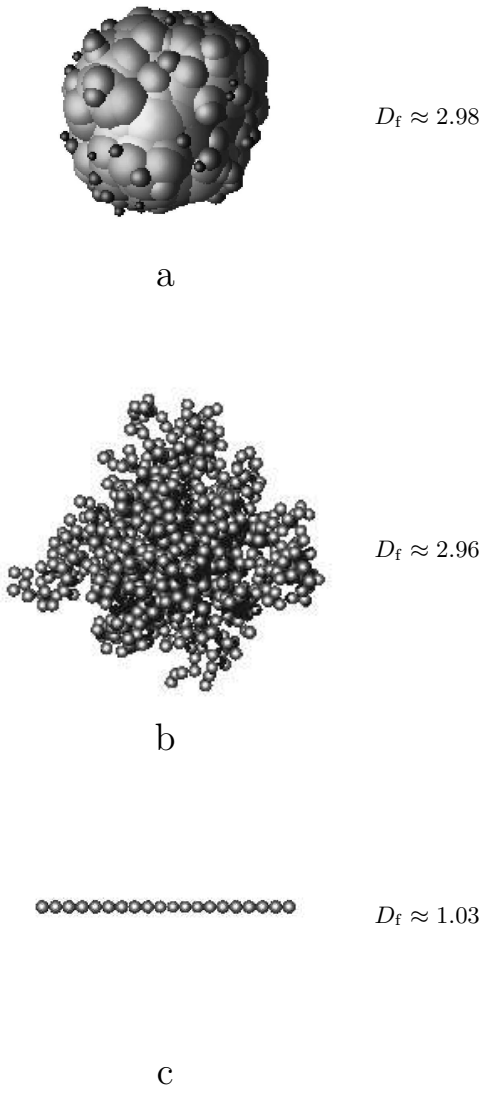

FIG. 2: Fractal dimension for 3 aggregates in $\mathbb{R}^3$: (a) 320 balls; (b) 1,500 balls; (c) 20 balls.

B. Aggregate spatial metrics

Instead of forcing a descriptor to conform to a predetermined set of criteria we will analyze the criteria and allow a shape descriptor to come forth naturally. We start from basic principles and analyze the aggregate using its volume and surface area. Volume, V, and surface area, S, are the most important and intuitive metrics. Most of the thermodynamic and chemical parameters of interest are related, one way or another, to one or both of these measures.

1. Volume and area

Our particle formation model initializes the collector aggregate as a single ball. The collector grows via collisions and surface deposition. As a result, V and S increase from their initial values. Considering the spherical geometry of the collector in its initial state we define

$$V_\mathrm{o} = \frac{4}{3}\pi R_\mathrm{o}^3 \ , \ S_\mathrm{o} = 4\pi R_\mathrm{o}^2 \tag{2}$$

and normalize V and S

$$v = \frac{V}{V_\mathrm{o}} \ , \ s = \frac{S}{S_\mathrm{o}}. \tag{3}$$

By construction, v and s are elements of the interval $[1, \infty]$.

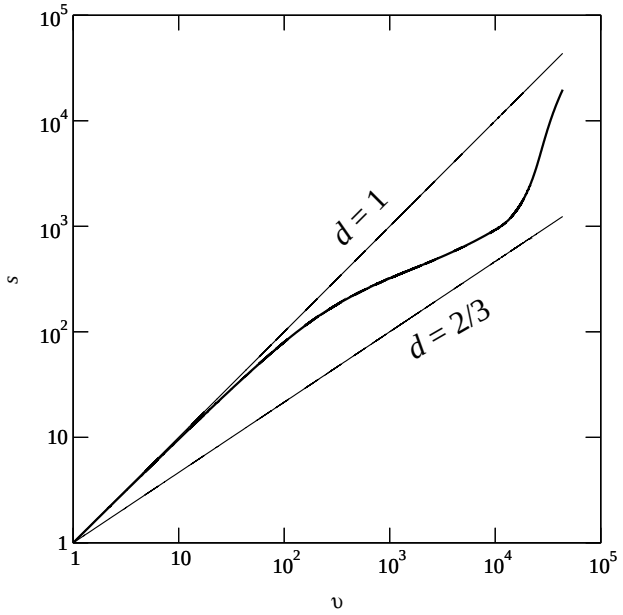

FIG. 3: Particle trajectory in $\ln v$–$\ln s$ space.

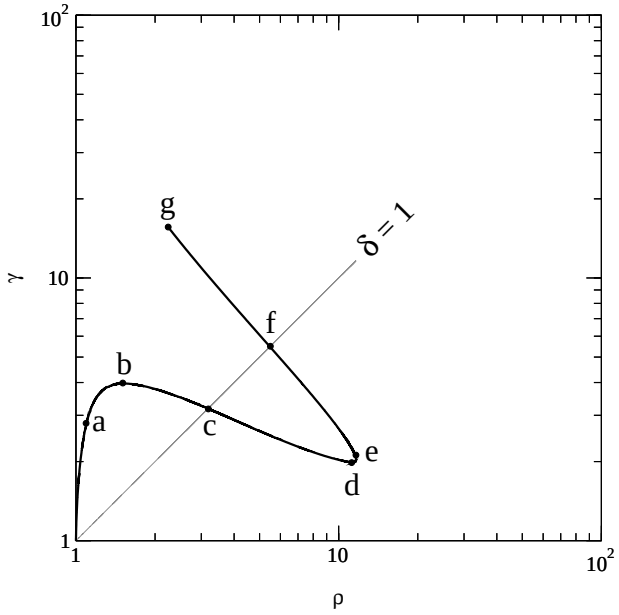

FIG. 4: Particle trajectory in $\ln \rho$–$\ln \gamma$ space.

2. *Particle trajectory in* $\ln v$–$\ln s$ *space*

Particle aggregation simulated under the influence of surface growth creates a particle trajectory in $\ln v$–$\ln s$ space, as illustrated in FIG. 3. Each simulation starts at $v = s = 1$. Thereafter, as v and s increase, the trajectory the particle follows in $\ln v$–$\ln s$ space is bounded, both above and below, by two limits. These two limits correspond to the lines in FIG. 3 with slopes $d = 1$ and $d = 2/3$.

The upper limit, $d = 1$, is the trajectory a particle would follow in the complete absence of surface growth. In this case, the collector grows solely from the addition of particles by collision, producing a chain-like aggregate composed of equally sized balls joined by point contacts (as, e.g., in FIG. 2b). In this limit

$$\frac{V}{V_\mathrm{o}} = n \quad \text{and} \quad \frac{S}{S_\mathrm{o}} = n, \tag{4}$$

implying

$$s = v. \tag{5}$$

In contrast, the lower limit, $d = 2/3$, is the trajectory encountered in the absence of collisions. Starting from a ball, the particle grows solely by surface deposition, retaining the spherical shape. In this limit

$$\frac{V}{V_\mathrm{o}} = \left(\frac{R}{R_\mathrm{o}}\right)^3 \quad \text{and} \quad \frac{S}{S_\mathrm{o}} = \left(\frac{R}{R_\mathrm{o}}\right)^2, \tag{6}$$

implying

$$s = v^{2/3}. \tag{7}$$

The two limits, $d = 1$ and $d = 2/3$, can be thought of as the maximum and minimum surface area bounds, respectively, for constant v. For example, holding volume fixed at $v = 10^3$ only allows surface area in the interval $s \in \left[10^2, 10^3\right]$ (see FIG. 3). An arbitrary trajectory, within the framework of the present model, can then be expressed by the curve [44]

$$s = v^d \ : \ d \in [2/3, 1]\,. \tag{8}$$

It is pertinent to mention that the particle trajectories examined in the present study are those developed through collisions of initially perfect spheres with simultaneously occurring growth of the encasing surface. While this mechanism covers a wide range of important applications, it is certainly not a universal description; for instance, one may encounter a different class of trajectories for a system of elongating rods.

3. *New trajectory space*

It is beneficial to analyze the particle trajectory in a new orthogonal coordinate system, shown in FIG. 4. It is obtained through a linear transformation of the fan-shaped region in FIG. 3, bounded by $d = 2/3$ and $d = 1$,

$$\begin{pmatrix} \sqrt{13}\,\ln\rho \\ \sqrt{18}\,\ln\gamma \end{pmatrix} = \begin{pmatrix} \sqrt{13} & -\sqrt{13} \\ -2\sqrt{2} & 3\sqrt{2} \end{pmatrix} \begin{pmatrix} \ln v \\ \ln s \end{pmatrix} \tag{9}$$

where $\rho = v/s$ and $\gamma = s/v^{2/3}$. In the literature [45, 46], the inverse of ρ and γ are referred to as *rugosity* and *globularity*, respectively.

The $\ln \rho$–$\ln \gamma$ analog to Eq. 8 is written

$$\gamma = \rho^\delta \ : \ \delta \in [0, \infty] \tag{10}$$

and exponents δ and d are related by the equation

$$\delta = \frac{d - 2/3}{1 - d}. \tag{11}$$

Perfectly spheroidal collector particles will have trajectories which start and stay on the ρ-axis, $\delta = 0$. Chain-like trajectories traverse the γ-axis and are identified by $\delta \to \infty$. Trajectories with $\delta = O(1)$ indicate collector particles which are neither balls nor chain-like.

δ is an aggregate shape descriptor satisfying our requirements. First and foremost, it differentiates between chain-like and spheroidal aggregates. It quantifies the amount of intersection between the constituent balls and provides a measure of roundness. For instance, the aggregate constructed from grossly intersected balls shown in FIG. 2a has $\delta \approx 0$ (FIG. 2a) and the chain-like aggregates in FIGS. 2b,c have $\delta \to \infty$. However, δ does not provide enough information on its own to determine if a particle is in a state of transition. In §III C we explore the transition and the role δ plays in it.

C. Transition from coalescence to fractal aggregation

The numerical value of δ provides a relative measure of the aggregate's position in $\ln\rho$–$\ln\gamma$ space. For instance, points **a**, **b**, and **g** on the trajectory depicted in FIG. 4 mark stages in the aggregate's morphology representative of chain-like particles. In contrast, points **d** and **e** are representative of spheroidal aggregates and **c** and **f** indicate a shape in between spheroidal and chain-like.

A transition from the coalescent regime to fully-developed fractal aggregation is characterized by a switch from $\delta < 1$ to $\delta > 1$, i.e., when the aggregate trajectory crosses the line $\delta = 1$. For the transition to be complete, i.e., when the aggregate remains near the chain-like or coalescent limit, the trajectory should move strongly away from one axis toward the other. For example, in FIG. 4 transition from the coalescent to the fractal limit begins somewhere between points **d** and **e** on the trajectory. In this region, the aggregate turns away from the ρ-axis and heads towards the $\delta = 1$ line. The transition is completed when the trajectory crosses over point **f** and continues on to **g**. An example of transition in the other direction, from the fractal to the coalescent limit, begins between the origin and point **b**, proceeds to point **c**, and is completed at point **d**.

To determine the direction of the transition, we consider the particle trajectory in yet another coordinate system, $\delta \equiv \ln\gamma / \ln\rho$ and

$$\Delta \equiv \frac{d(\ln\gamma)}{d(\ln\rho)} = \frac{D - 2/3}{1 - D}, \tag{12}$$

where

$$D \equiv \frac{d(\ln s)}{d(\ln v)}. \tag{13}$$

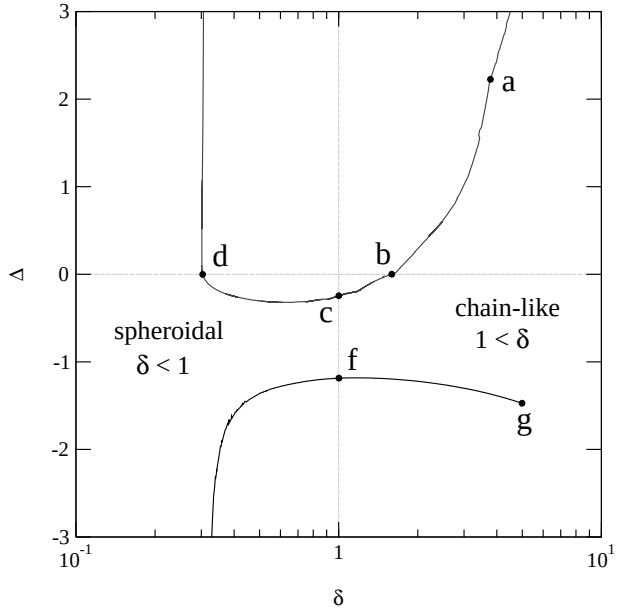

FIG. 5: Particle trajectory in δ–Δ space. The points **a**–**g** correspond to the points **a**–**g** of FIG. 4. The trajectory traverses the points in order. It encounters point **a** first and ends on point **g**.

It is interesting to note the similarity between Eq. 12 and Eq. 11.

The particle trajectory in δ–Δ space is shown in FIG. 5. Recall that the transition from the fractal to the coalescent limit begins as the trajectory approaches point **a** and continues to **b**. The trajectory in this region is characterized by $\delta > 1$ and the particles are chain-like aggregates. In FIG. 5 we see that Δ decreases from positive values to 0 at point **b**. From point **b**, Δ remains negative and δ continues to decrease until it reaches a value of 1 at point **c**. This is our *middle* point where the particle is neither chain-like nor spheroidal. The trajectory proceeds to point **d** where $\delta < 1$ and $\Delta = 0$.

Similarly, the transition from coalescence to chain-like aggregates begins between points **d** and **e**. In this region, $\delta < 1$, Δ passes from 0 to ∞, and the particles are spheroidally shaped. Point **e** is not shown in FIG. 5 since $\Delta = \infty$. After passing point **e**, Δ becomes negative. The trajectory crosses $\delta = 1$ at point **f** and once again the particle is neither chain-like nor spheroidal. Δ remains negative, the trajectory continues to point **g**, and the particle ends chain-like with $\delta > 1$.

The method of using (δ, Δ) to predict the transition will be referred to as the *delta-and-Delta* method or `DAD`. It is δ which reveals where in $\ln v$–$\ln s$ space the trajectory is and Δ which reveals the trajectory direction. While it is a switch in δ across the line $\delta = 1$ which dictates *if* transition occurs, it is a switch in the sign of Δ which determines *where* in $\ln v$–$\ln s$ space it starts and ends.

IV. ANALYSIS OF THE TRANSITION

A. Four simulation scenarios

To examine the transition, Monte Carlo simulations were conducted using four scenarios. In each case, DADis used to analyze the transition. While the DADmethod is applicable to any system of aggregating matter, to make our analysis more concrete, we consider soot particle formation in the environment of a 10-bar laminar premixed flame of ethylene. Specifically, the performed tests utilized [44] the rates of particle collisions, surface growth, and nucleation taken from Flame 2 of Ref. [43]. We begin with a benchmark case, considering particle collisions without surface growth. Then two cases that idealize and test the influence of particle nucleation are examined. We conclude with a more realistic test.

1. Scenario 0: benchmark

We start with particle aggregation in the absence of surface growth, a regime researched extensively in past studies [34, 36, 38, 51]. It will be referred to as *Scenario 0* (S0).

105 collector particles with 1,000 balls each were constructed using the Monte Carlo algorithm described in §II. In this scenario, the candidate particles in the Environment remain at a constant size for the duration of the simulation. At the conclusion, S0 creates an aggregate from a union of equally sized balls with no intersection. The aggregate fractal behavior was analyzed in terms of Eq. 1. In agreement with previous studies, the power law dependence ensues for n in the range 10–100 for the conditions set by S0. D_{f} is taken as the asymptotic slope of a $\log R_{\mathrm{g}}$ versus $\log n$ plot as shown in FIG. 6. D_{f} obtained from S0 is 2.97 ± 0.07, which agrees favorably with that reported by Meakin [39], 3.09 ± 0.19.

The S0 particle trajectory in $\ln\rho$–$\ln\gamma$ space, consistent with the definition of S0, remains on the γ-axis since the particles formed are chain-like aggregates with no intersection between balls. FIG. 7 shows snapshots of collector particles generated by S0 at $\gamma = 1, 3, 7, 10$. Each snapshot is accompanied by the number of balls, the collision radius R_{c}, and the DADvalues (δ, Δ). R_{c} is related to R_{g} by $R_{\mathrm{g}} = (3/5)^{1/2} R_{\mathrm{c}}$ so that in the limit of a perfectly spherical particle, the collision and particle radii become equal. At each point, S0 has produced classic chain-like aggregates with easily identifiable balls. In addition, each particle exhibits shape descriptors with value $(\delta, \Delta) = (\infty, \infty)$. In other words, S0 experiences no transition.

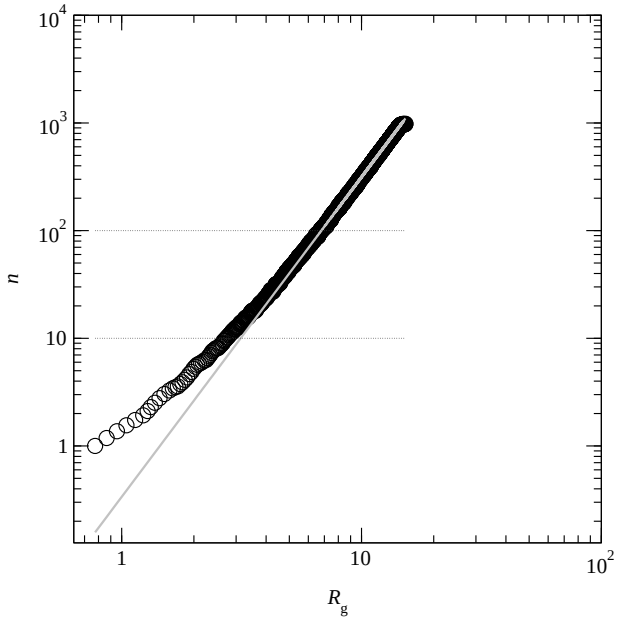

FIG. 6: The dependence of n on R_{g} for 105 collector particles with 1,000 balls each. Power law dependence is attained for n in the range 10–100.

2. Scenario 1: surface growth applied to the collector and candidate

Aggregation with simultaneous surface growth was analyzed next using *Scenario 1* (S1). 71 collector particles with 1,350 balls each were constructed using the Monte Carlo algorithm described in §II. S1 candidate particles are exposed to the same surface growth effects as the collector particle. That is, the radii of the candidate particles in the Environment grow at the same rate as the radii of the union of balls in the aggregate. The final result is a collector particle constructed from heavily intersected, equally sized balls. S1 assumes that the candidate particle represents an ensemble average, increasing in size through surface growth.

The S1 particle trajectory in $\ln\rho$–$\ln\gamma$ space is shown in FIG. 8. We see that instantaneously after leaving the origin, the trajectory departs from the γ-axis. This indicates that minute amounts of intersection between the aggregate's balls exist. At this early stage in the particle morphology, surface growth already exerts its influence. However, since the trajectory is still prominently set in the region $\delta > 1$, the aggregate is still strongly chain-like. Indeed, examination of the snapshot of a representative particle at point **a**, shown in FIG. 9a, reveals a chain-like aggregate similar to the ones created by S0. At point **a** the trajectory slope is equal to the slope of the $\delta = 1$ line.

An infinitesimal distance past **a** and surface deposition has altered the trajectory and reduced the slope to $\Delta < 1$. At this point, if the slope remains constant, the trajectory will inevitably intersect the $\delta = 1$ line.

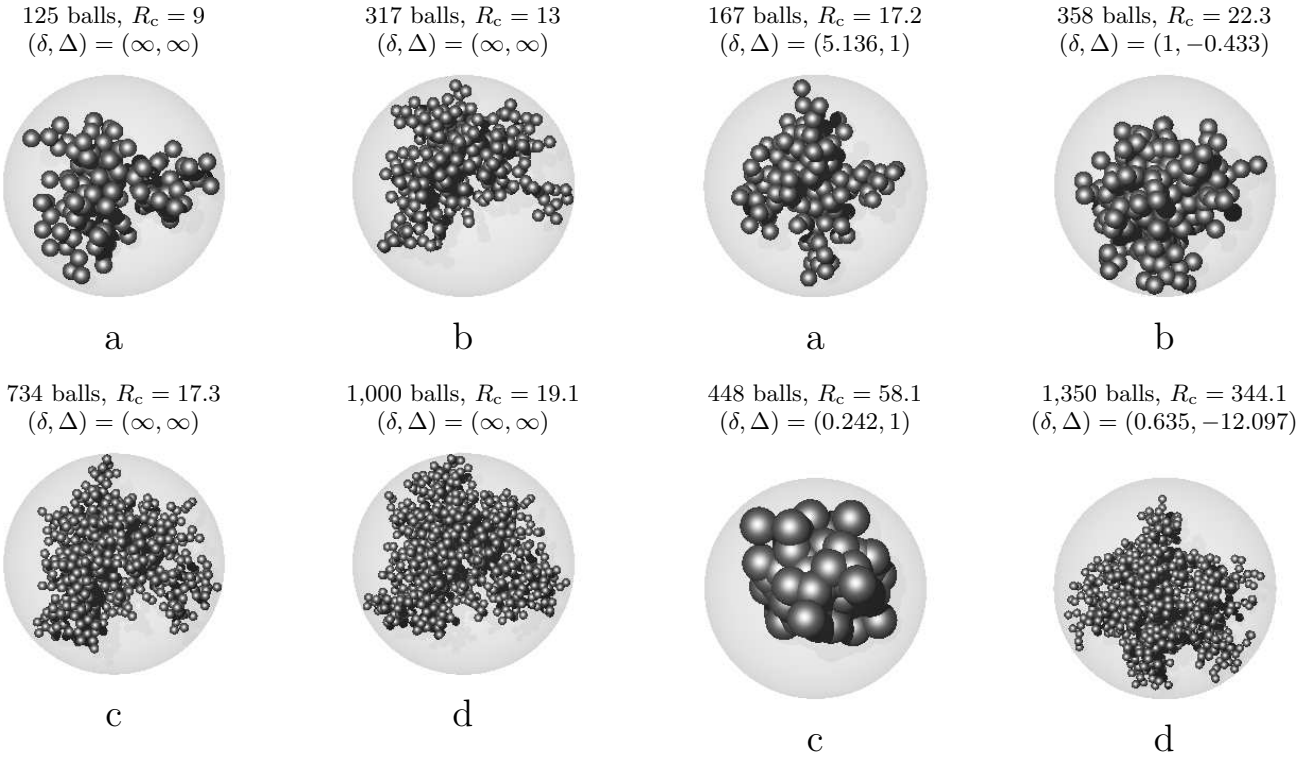

FIG. 7: Snapshots of collector particles created using Scenario 0.

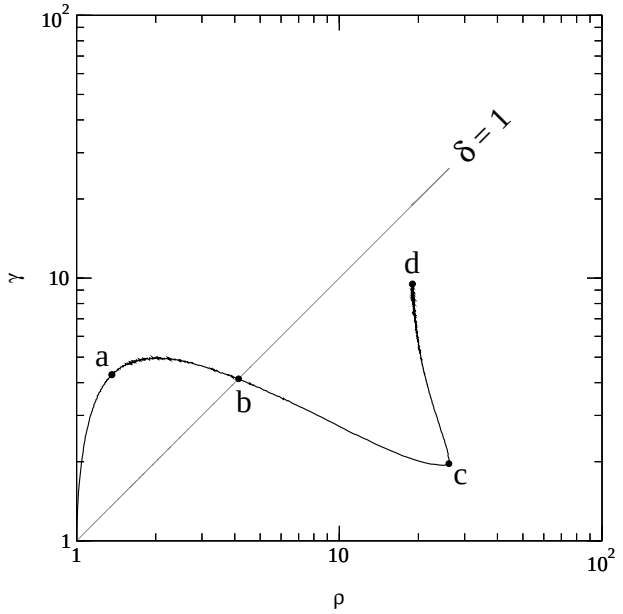

FIG. 8: Scenario 1 particle trajectory in $\ln \rho$–$\ln \gamma$ space.

However, Δ continues to decrease, passes through zero to negative values, and intersects the $\delta = 1$ line at point **b**. Here, the particle is neither chain-like nor spheroidal. The snapshot shown in FIG. 9b depicts an aggregate with heavy intersection yet with chain-like characteristics in its extremities. Thus, the overall shape of the particle is influenced by both surface growth and addition of particles via collision.

FIG. 9: Snapshots of collector particles created using Scenario 1. The snapshots correspond to the points **a**–**d** of FIG. 8.

After the trajectory departs from point **b** it enters the region $\delta < 1$. The slope remains negative then increases to zero. Eventually the trajectory reaches point **c** where Δ is one and again parallel to the $\delta = 1$ line. At **c**, the trajectory is close to its maximal distance from the $\delta = 1$ line in the coalescent region of $\ln \rho$–$\ln \gamma$ space. At this stage on the trajectory, the geometric appearance of the particle is dominated by the effects of surface deposition and has attained its most spheroidal shape. FIG. 9c shows a compact collector with advanced stages of intersection between each ball. It is remarkable that this snapshot shows a collector constructed from a union of 448 balls. In fact, visual comparison of FIGS. 9b and 9c could lead one to the incorrect assumption that the aggregate in FIG. 9b is constructed from a larger number of balls.

From **c** the trajectory moves quickly towards the $\delta = 1$ line. This implies that surface growth is losing its dominance and collisions are equally influential in determining the aggregate shape. The S1 simulation was terminated at point **d** with a value of $\delta = 0.635$. The snapshot shown in FIG. 9d looks very similar to the one shown in FIG. 9b but larger and formed with more balls. It shows heavy intersection at the core but with chain-like characteristics in its extremities. This is expected since both particles

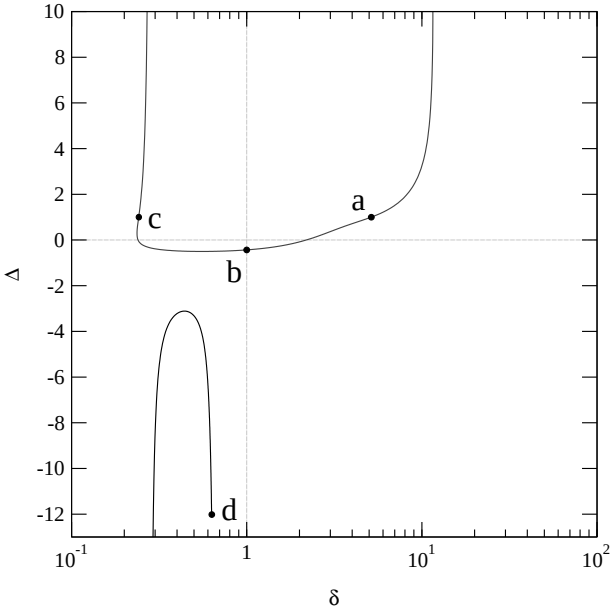

FIG. 10: Particle trajectory in DADspace. The points **a**–**d** have a 1–to–1 correspondence with the points **a**–**d** of FIG. 8. The trajectory traverses the points in order, encountering point **a** first and ending on point **d**.

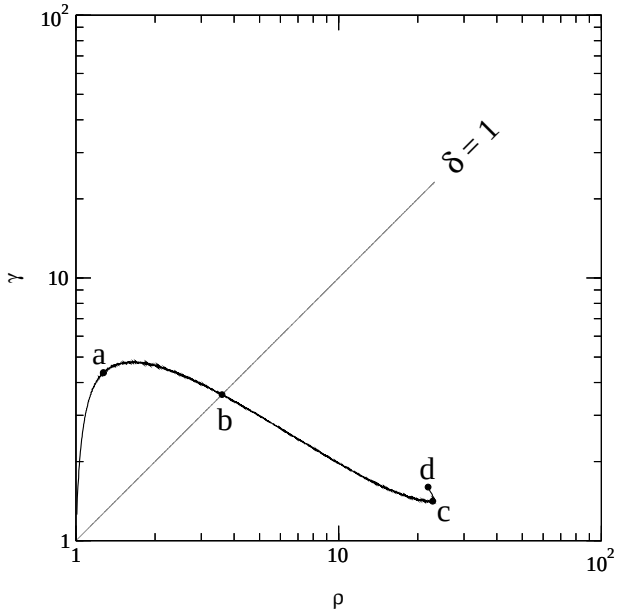

FIG. 11: Scenario 2 particle trajectory in $\ln\rho$–$\ln\gamma$ space.

reside on or near the $\delta = 1$ line.

The S1 trajectory in DADspace is shown in FIG. 10. S1, like S0, begins with DADvalues $(\delta, \Delta) = (\infty, \infty)$. Both shape descriptors decrease until they reach values of $(\delta, \Delta) = (5.136, 1)$ at **a**. The collector transitions from fractal-like aggregation to coalescence between **a** and **c**. At **c** FIG. 10 reveals that the collector is in fact near its maximal distance from $\delta = 1$ in the coalescent stage of its morphology. In the region near **c**, the collector should be at its most spheroidal. Transition back to fractal-like aggregation begins once the trajectory departs from **c**. At **d** the transition remains incomplete but is headed toward the $\delta = 1$ line.

3. Scenario 2: surface growth applied to the collector only

The next scenario is *Scenario 2* (S2). 95 collector particles with 1,200 balls each were constructed using the Monte Carlo algorithm described in §II. In contrast to the last scenario, S2 keeps the candidate radii constant for the duration of the simulation. S2 simulates aggregation at the peak of particle inception when rapid nucleation results in a vast supply of candidate particles. In this regime, the population of particles in the Environment is dominated by newly incepted monomers [42]. As a result, the collector particle experiences the majority of its collisions with small, freshly nucleated particles.

The S2 collector particle trajectory is shown in FIG. 11. The character of the trajectory for S2 in $\ln\rho$–$\ln\gamma$ space is extremely similar to the one for S1. Instantaneously after leaving the origin, the trajectory also departs from the γ-axis. Again, this is an indication that there exists intersection between the aggregate's balls. A snapshot of a representative particle at point **a** is shown in FIG. 12a and reveals a chain-like aggregate which looks rather like the one shown in FIG. 9a. Each representative particle **a**–**d** shown in FIG. 12 is chosen based on the same criteria as those in FIG. 9. At point **a**, the slope is equal to one, at **b** the trajectory intersects the $\delta = 1$ line, at **c** the collector is at its most spheroidal, and at **d** the simulation concludes. Visually, the particles displayed at points **a** and **b** are extremely similar to their counterparts in FIG. 9. At point **a** in either scenario, the collectors appear chain-like with distinct, easily identifiable balls. The collectors at **b**, although different in overall size, have the same visual appearance. They both are between chain-like and spheroidal in shape with heavy intersection at their cores but with chain-like characteristics in their extremities. At **c** the snapshot shows a compact collector with advanced stages of intersection between each ball. S2 is much more spheroidal at this point than S1 since the candidate particles remain small for the duration of the simulation and are more readily covered by surface deposition. Since the collector attains its most spheroidal shape and the coalescent regime is at its zenith at point **c**, it is probable that the collector in FIG. 12c is what referred to in the literature as composed of "primary" particles.

The trajectory moves quickly away from point **c** towards the $\delta = 1$. S2 concludes at point **d** with a value of $\delta = 0.144$. It is interesting to compare the snapshot shown in FIG. 12d to the one in FIG. 9c. Since the S2 value of δ at **d** is less than the one for S1 at **c** we could conclude that the S2 snapshot will be rounder. Comparison of the two confirms that this is indeed the case.

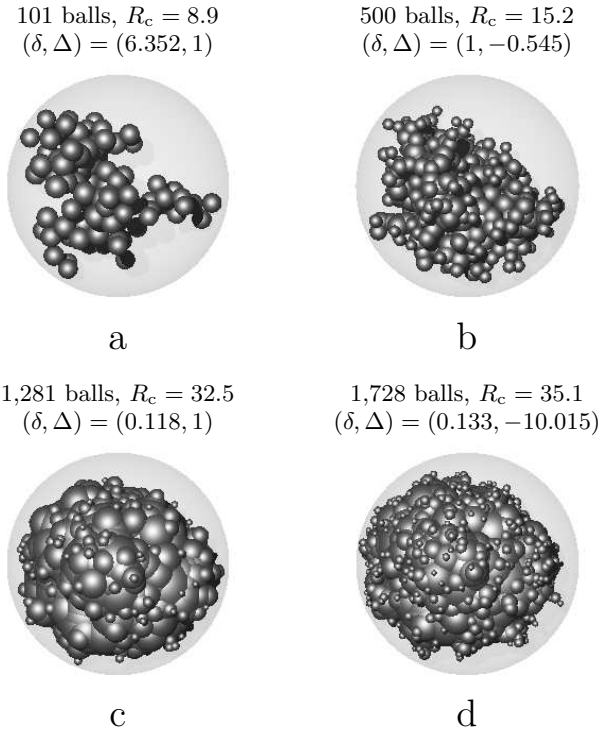

FIG. 12: Snapshots of collector particles created using Scenario 2. The snapshots correspond to the points **a**–**d** of FIG. 11.

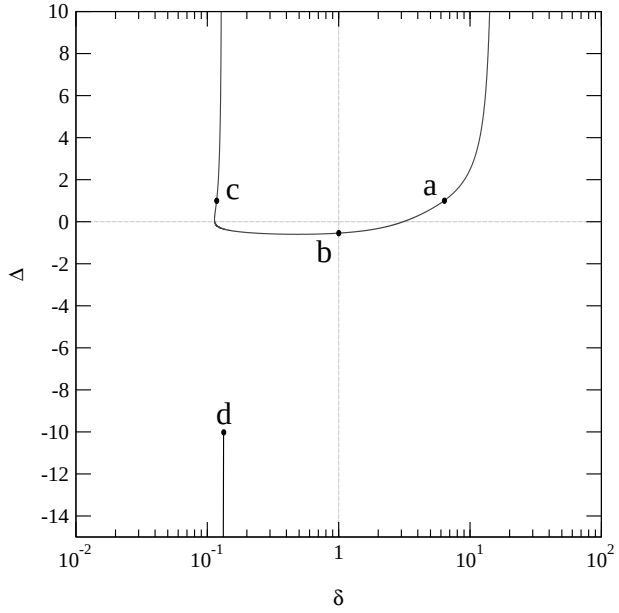

FIG. 13: Particle trajectory in DADspace. The points, **a**–**d**, have a 1–to–1 correspondence with the points, **a**–**d**, of FIG. 11. The trajectory traverses the points in order, encountering point **a** first and ending on point **d**.

The S2 trajectory in DADspace is shown in FIG. 13. Starting at $(\delta, \Delta) = (\infty, \infty)$ the shape descriptors decrease to $(\delta, \Delta) = (6.352, 1)$ at point **a**. Like S1, the collector transitions from fractal-like aggregation to the coalescent regime between **a** and **c** and concludes at **c**. FIG. 13 shows that at **c** the collector is near its maximal distance from the $\delta = 1$ line. In this region, the collector is at its most spheroidal. Departing from **c**, the particle transitions back to a chain-like shape and approaches the $\delta = 1$ line.

4. A simple test scenario

Scenarios S1 and S2 examine the transition between the two coagulation regimes of candidate particle growth. We now turn to a test scenario (ST) designed [44] to mimic more realistic growth rates of candidate particles, characteristic of soot particles nucleating in a 10-bar laminar premixed flame of ethylene [43]. These Monte Carlo simulations were conducted at the following set of conditions: constant temperature; step-function nucleation and surface-growth rates; and collector radius increasing proportionally to the cube root of time [44]. This is a simplified representation of the flame results obtained by Kazakov *et al.* [43].

Under this scenario, 130 collector particles were constructed with 550 Balls each. A typical ST particle trajectory in $\ln \rho$–$\ln \gamma$ space is shown in FIG. 14, and representative snapshots of collector particles, at the same four points **a**–**d** as in scenarios S0–S2, are displayed in FIG. 15.

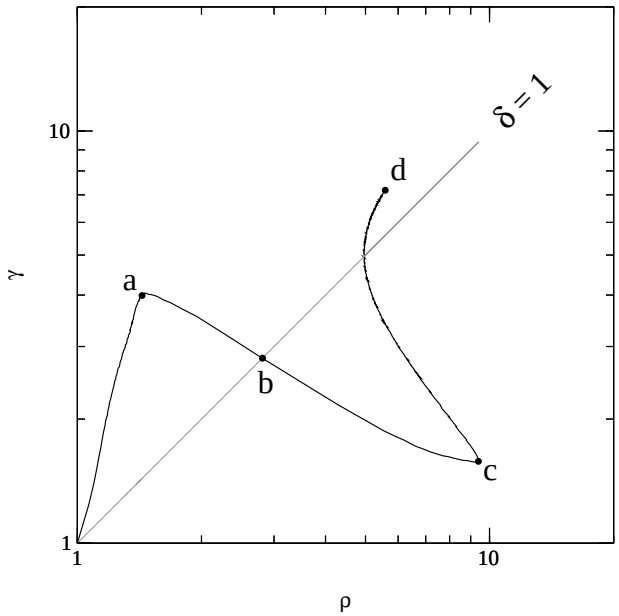

FIG. 14: Test scenario particle trajectory in $\ln \rho$–$\ln \gamma$ space.

The trajectory in FIG. 14 reveals a collector particle morphology that exhibits two distinct transitions, fractal-to-coalescent and coalescent-to-fractal. The snapshot shown in FIG. 14a represents the start point of the fractal-to-coalescent transition and is strongly chain-like.

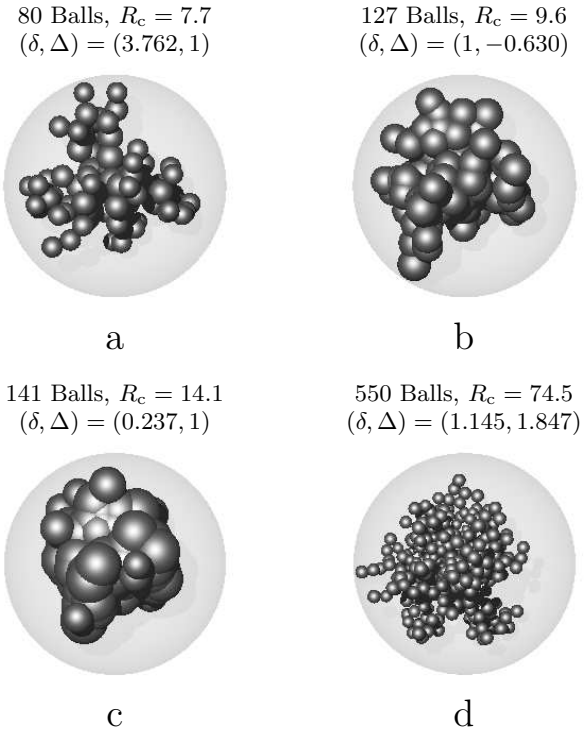

FIG. 15: Snapshots of collector particles created using the test scenario. The snapshots correspond to the points **a**–**d** of FIG. 14.

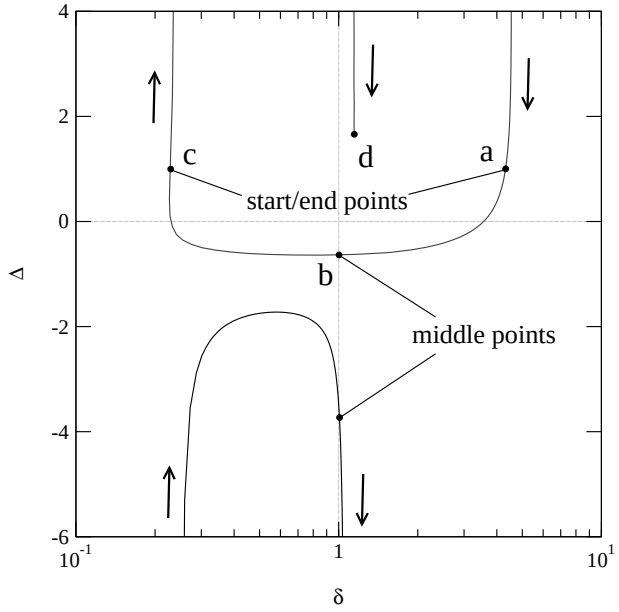

FIG. 16: Particle trajectory in DADspace. The points, **a**–**d**, have a 1–to–1 correspondence with the points, **a**–**d**, of FIG. 14. The trajectory traverses the points in order, encountering point **a** first and ending on point **d**.

It is characterized by $(\delta, \Delta) = (3.762, 1)$ and is consistent with the DADimplementation used to detect the different stages of the transition. Figures 14b and c show snapshots of representative collector particles taken at the middle and end points, respectively. The collector shown in FIG. 14b is in a transitory state between chain-like and spheroidal. Figure 14c shows a spheroidal collector at point **c** with DADvalues $(\delta, \Delta) = (0.237, 1)$. While it actually has 14 more balls, visually, the particle at **c** appears to be constructed from less balls than the one at **b**. Point **c** corresponds to the start point of the coalescent-to-fractal transition. The final snapshot is of a chain-like collector particle taken at point **d** and with DADvalues $(\delta, \Delta) = (1.145, 1.847)$.

The ST trajectory in DADspace is shown in FIG. 16. The trajectory unambiguously detects where each transition begins and ends. For example, the start and end points of fractal-to-coalescent and coalescent-to-fractal transitions are easily found where the trajectory crosses $\Delta = 1$. The middle points of the transition are found at $\delta \approx 1$.

V. DISCUSSION

The simulations demonstrate that the morphology of aggregating particles is dependent on both the surface deposition and particle nucleation rates. In all three scenarios, S1, S2 and ST, intense nucleation, which occurs early in the particle morphology [42, 44], forces particles to remain fractal-like in shape. This is due to similarly sized aggregating material—in this case, the candidate and collector particles.

Stated another way, early in the particle lifecycle, nucleation is intense resulting in a cloud of tiny candidate particles. Therefore, the vast majority of early collisions occur between small particles. The size of the collector is comparable to the size of the candidate particles. Collisions are occurring too fast for surface deposition to cover particles added on the collector surface via aggregation and the resultant shape remains fractal-like. This is evident from the young collector particles depicted in FIGS. 9b, 12b, and 15b.

Later in the lifecycle the shape of the collector particle is less influenced by nucleation and more influenced by surface deposition. As the rate of surface deposition increases and nucleation wanes, the candidate particles are less able to effect change on the geometry of the collector. As surface deposition becomes the dominant mechanism we transition from fractal-like to coalescent growth. Eventually, we obtain particles similar to those shown in FIGS. 9c, 12c, and 15c.

In the advanced stages of the lifecycle, when surface deposition is waning, particle morphology is again influenced by collisions as aggregation re-asserts itself. Geometric effects due to aggregation dominate and another transition, this time from the coalescent to fractal-like regime, occurs. Figures 9d and 15d show particles indicative of this phase in the lifecycle.

It is interesting to note the effect of nucleation on the evolution of particle morphology. When the Environ-

ment is dominated by a cloud of tiny candidate particles, in the presence of surface growth, the model generates the roundest particles. The extreme of such behavior was simulated by scenario S2 when the candidate particles were kept at an artificially small and constant size. This regime mimics the presence of a strong nucleation source, supplying copious amounts of the tiniest particles [17]. Indeed, the collector produced in scenario S2 has the most spheroidal shape, as illustrated in FIG. 12. Scenario ST, with a time-dependent size of candidate particles, passed through a similar phase, as demonstrated by the collector shown in FIG. 15c.

VI. SUMMARY

A dynamic Monte Carlo method was used to simulate particle aggregation with simultaneous surface growth. The transition between the coalescent and the fully-developed aggregation regimes was examined.

Examination of the transition necessitated the development of shape descriptors to quantify the geometric differences between particles. The descriptors δ and Δ were developed to accomplish this task. Descriptor δ was used to quantify a particle's geometric proximity to either a perfectly round ball or a chain-like aggregate. For a given shape, Δ was used to quantify a particle's direction of geometric change. This method of using δ and Δ, called `DAD`, was implemented successfully throughout the study.

Using `DAD`to quantify particle morphology facilitated analysis of and led to a working definition for the transition. The definition formulated was completely characterized by δ and Δ. Evaluation of these two parameters determined the state of the particle.

Most revealing is the demonstration of the intimate dependence exhibited by the particle morphology on both the surface deposition and particle nucleation rates. The results show that particle aggregation is not separated in time from particle nucleation, as is often presumed.

Acknowledgments

The research was supported by the Director, Office of Energy Research, Office of Basic Energy Sciences, Chemical Sciences Division of the U.S. Department of Energy, under Contract No. DE-AC03-76SF00098.

[1] J. H. Seinfeld and S. N. Pandis, *Atmospheric Chemistry and Physics. From Air Pollution to Climate Change* (Wiley, New York, 1998).
[2] S. K. Friedlander, *Smoke, Dust and Haze* (Oxford, New York, 2000).
[3] B. S. Haynes and H. G. Wagner, Prog. Energy Combust. Sci. **7**, 229 (1981).
[4] H. Bockhorn, editor, *Soot Formation in Combustion: Mechanisms and Models* (Springer-Verlag, Berlin, 1994).
[5] J. S. Mathis, Annu. Rev. Astron. Astrophys. **28**, 37 (1990).
[6] W. M. Irvine, Origins Life Evolution Biosphere **28**, 365 (1998).
[7] K. Kinoshita, *Carbon. Electrochemical and Physicochemical Properties* (Wiley, New York, 1988).
[8] S. E. Pratsinis, Prog. Energy Combust. Sci. **24**, 197 (1998).
[9] S. N. Rogak, R. C. Flagan, and H. V. Nguyen, Aerosol Sci. Technol. **18**, 25 (1993).
[10] Ü. Ö Köylü, G. M. Faeth, T. L. Farias, and M. G. Calvalho, Combust. Flame **100**, 621 (1995).
[11] A. V. Philippov, M. Zurita, and D. E. Rosner, J. Colloid Interface Sci. **229**, 261 (2000).
[12] C. M. Sorensen, Aerosol Sci. Technol. **35**, 648 (2001).
[13] M. V. Smoluchowski, Z. Phys. Chem. **92**, 129 (1917).
[14] N. A. Fuchs, *The Mechanics of Aerosols* (Dover, Mineola, NY, 1989).
[15] M. Frenklach and H. Wang, in *Soot Formation in Combustion: Mechanisms and Models*, edited by H. Bockhorn (Springer-Verlag, Berlin, 1994), p. 165.
[16] R. A. Dobbins and G. W. Mulholland, Combust. Sci. Technol. **40**, 175 (1984).
[17] M. Frenklach and S. J. Harris, J. Colloid Interface Sci. **118**, 252 (1987).
[18] J. D. Landgrebe and S. E. Pratsinis, Ind. Eng. Chem. Res. **28**, 1474 (1989).
[19] M. K. Alam, and R. C. Flagan, Aerosol. Sci. Technol. **5**, 237 (1986).
[20] B. S. Haynes and H. G. Wagner, Z. Phys. Chem. N. F. **133**, 201 (1982).
[21] M. Frenklach, Phys. Chem. Chem. Phys. **4**, 2028 (2002).
[22] G. Ulrich and N. S. Subramanian, Combust. Sci. Technol. **17**, 119 (1977).
[23] W. Koch and S. K. Friedlander, J. Colloid Interface Sci. **140**, 419 (1990).
[24] G. Prado, J. Jagoda, K. Neoh, and J. Lahaye, Proc. Combust. Inst. **18**, 1127 (1981).
[25] G. Prado and J. Lahaye, in *Particulate Carbon: Formation During Combustion*, edited by D. C. Siegla and G. W. Smith (Plenum, New York, 1981), p. 143.
[26] Y. Xiong and S. E. Pratsinis, J. Aerosol Sci. **24**, 283 (1993).
[27] Y. Xing and D. E. Rosner, Mat. Res. Soc. Symp. Proc. **457**, 167 (1997).
[28] R. A. Dobbins, Combust. Flame **130**, 204 (2002).
[29] M. R. Zachariah and M. J. Carrier, J. Aerosol Sci. **30**, 1139 (199).
[30] M. R. Zachariah, M. J. Carrier, and E. Blaisten-Barojas, J. Phys. Chem. **100**, 14856 (1996).
[31] B. L. Wersborg, J. B. Howard, and G. C. Williams, Proc. Combust. Inst. **14**, 929 (1973).
[32] J. B. Howard and J. P. Longwell, in *Polynuclear Aromatic Hydrocarbons: Formation, Metabolism, and Measuments*, edited by M. Cooke and A. J. Dennis (Battelle, Columbus, OH, 1983), p. 27.
[33] G. W. Smith *Soot in Combustion Systems and Its Toxic*

Properties, edited by J. Lahaye and G. Prado (Plenum, New York, 1983), p. 163.
[34] M. J. Vold, J. Colloid Sci. **18**, 684 (1963).
[35] R. Jullien and R. Botet, *Aggregation and Fractal Aggregates* (World Scientific, Singapore, 1987).
[36] P. Meakin, Phys. Rev. A **27**, 604 (1983).
[37] P. Meakin, in *The Fractal Approach to Heterogeneous Chemistry*, edited by D. Avnir (Wiley, New York, 1989), p. 131.
[38] G. W. Mulholland, R. J. Samson, R. D. Mountain, and M. H. Ernst, Energy Fuel **2**, 481 (1988).
[39] P. Meakin, J. Colloid Interface Sci. **96**, 415 (1983).
[40] R. A. Dobbins and C. M. Megaridis, Appl. Optics **30**, 4747 (1991).
[41] Ü. Ö Köylü and G. M. Faeth, J. Heat Transfer **116**, 152 (1994).
[42] P. Mitchell and M. Frenklach, Proc. Combust. Inst. **27**, 1507 (1998).
[43] A. Kazakov and M. Frenklach, Combust. Flame **114**, 484 (1998).
[44] P. Mitchell, Ph.D. thesis, University of California, Berkeley (2001).
[45] A. Y. Meyer, J. Comput. Chem. **9**, 18 (1988).
[46] G. A. Arteca, Int. J. Quant. Chem. **70**, 981 (1998).
[47] A. Kazakov, H. Wang, and M. Frenklach, Combust. Flame **100**, 111 (1995).
[48] M. K. Wu and S. K. Friedlander, J. Aerosol Sci. **24**, 273 (1993).
[49] C. M. Megaridis and R. A. Dobbins, Combust. Sci. Technol. **63**, 153 (1989).
[50] V. Ossenkopf, Astron. Astrophys. **280**, 617 (1993).
[51] A. Gutsch, S. Pratsinis, and F. Löffler, J. Aerosol Sci. **26**, 187 (1995).
[52] M. Frenklach and H. Wang, Proc. Combust. Inst. **23**, 1559 (1991).